A Generalized Analysis for Grid Oscillator Design

Scott C. Bundy, *Student Member, IEEE*, and Zoya B. Popović

***Abstract*—A full-wave analysis of infinite periodic grid structures loaded with active devices is presented. The grid consists of arbitrary periodic metal patterns printed on one or both sides of a dielectric slab in free space. Since the structure is periodic, under equi-phase conditions it is sufficient to analyze a single unit cell. An expression is derived relating the radiated electric field to the surface current density on the metal, which is determined by the method of moments. The driving-point impedances are found for any active devices embedded in the grid structure. Using this analysis, the metal geometry can be optimized for designing active quasi-optical power-combining grids for the microwave and millimeter-wave regions.**

I. Introduction

FREE-SPACE power-combining techniques for the microwave and millimeter-wave regions demonstrated to date are 1) grid oscillators and amplifiers [1], [2], and 2) active resonant antennas, such as patches or slots that incorporate oscillator or amplifier circuits [3]–[5]. The largest number of combined devices was achieved in grid oscillators, in which a metal mesh loaded with 100 MESFET's was placed in a Fabry-Perot cavity [6]. This method was first proposed and the field modes theoretically investigated for the case of a confocal resonator with one planar mirror [7]. For a power combiner design, it is convenient to use a circuit model in which the active device is embedded. Such a circuit model, for which the elements are found using an EMF analysis, was presented in [6], [8]. This analysis is subject to certain approximations and is not valid for an arbitrary metal geometry of the grid structure, but is adequate for grids in which the active device terminals are connected to thin metal strips [6], [8]. However, as demonstrated in [9] by comparing a thin-strip grid oscillator with a bow-tie grid, the metal geometry significantly affects the behavior of the grid power combiner. Further, the work presented in [9] demonstrates the feasibility of quasi-optical systems consisting of grids printed on opposite sides of the same substrate, or stacked in each other's near fields. For example, a grid of varactor diodes was fabricated on the back side of a MESFET grid oscillator and demonstrated 10% electrical frequency tuning with less than 2 dB change in power.

The goal of the work presented in this paper is a design-oriented analysis of a generalized periodic active grid oscillator power combiner. The grid can have a three-terminal power-generating device on one side of an arbitrarily thick dielectric, and another device, such as a varactor or *pin* diode or another transistor, on the back side. Further, the shape of the grid metallization is arbitrary. To analyze the grid, a Fortran program based on full-wave theory was written for a personal computer. The results compare favorably with measurements and other theories for several well-known geometries. Examples of analysis and measurements of passive meshes are presented, as well as design and experimental data for transistor grid oscillators.

Manuscript received March 28, 1994; revised June 17, 1994. This work was supported in part by the National Science Foundation under a Research Initiation Award, and in part by the Army Research Office under contract #DAAL03-92-G-0265.

The authors are with the University of Colorado, Department of Electrical and Computer Engineering, Boulder, Colorado 80309 USA.

IEEE Log Number 9405436.

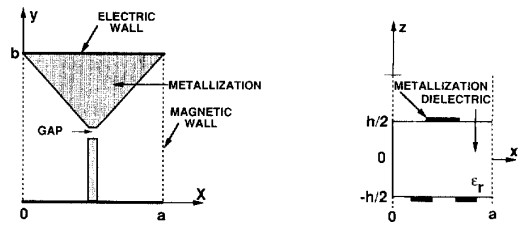

Fig. 1. (a) Top view and (b) side view of a unit cell geometry with metallization on both sides of the dielectric. The active device is placed across the gap.

II. Full-Wave Analysis of Loaded Periodic Grid Structures

A quasi-optical power-combining grid consists of an array of active devices which load a periodic metal pattern printed on a dielectric substrate. In this analysis, it is assumed that the periodic grid structure is infinite in both the x and y directions, and that the solid-state devices operate in phase. Under these conditions, the behavior of the entire grid may be analyzed on the basis of a single unit cell, whose electric and magnetic wall boundaries arise from the symmetry of the currents. In the following analysis, arbitrary metallization is allowed on one or both sides of the dielectric, as long as the pattern is periodic and the unit cell boundary conditions are preserved. Fig. 1 shows top and side views of a unit cell with metallization on both sides of the dielectric. For a grid oscillator, an active device is placed in the gap of the metal structure. To predict the behavior of the power combiner, it is important to know the driving-point impedance presented to the active device terminals. This impedance is determined by a full-wave analysis using the method of moments. An analytical relationship between the tangential electric field and the surface current density on both dielectric interfaces is derived. A time-harmonic voltage generator representing the active device is placed in the gap, producing a constant electric field in the small region of the gap. The current density on the

metallization and in the gap is then expanded as a summation of rooftop basis functions, and Galerkin's method is applied to find the current. The ratio of the voltage across the gap to the current through the gap is the driving-point impedance seen by the device. In the program, this entire analysis is performed over a range of frequencies.

A. Derivation of the Green's Function

To satisfy the boundary conditions enforced by the electric and magnetic walls in Fig. 1, the tangential electric fields in any plane of constant z can be expanded in Fourier series

$$E_x(x,y,z) = \sum_{m=1}^{\infty}\sum_{n=1}^{\infty} E_{mnx}(z) \times \sin\left(\frac{m\pi x}{a}\right)\sin\left(\frac{n\pi y}{b}\right) \quad (1)$$

$$E_y(x,y,z) = \sum_{m=0}^{\infty}\sum_{n=0}^{\infty} E_{mny}(z) \times \cos\left(\frac{m\pi x}{a}\right)\cos\left(\frac{n\pi y}{b}\right) \quad (2)$$

where a is the width and b is the height of the unit cell. Since the currents generating the fields are periodic, on each side of the dielectric they may also be expressed as Fourier series

$$J_x(x,y) = \sum_{m=1}^{\infty}\sum_{n=1}^{\infty} J_{mnx} \times \sin\left(\frac{m\pi x}{a}\right)\sin\left(\frac{n\pi y}{b}\right) \quad (3)$$

$$J_y(x,y) = \sum_{m=0}^{\infty}\sum_{n=0}^{\infty} J_{mny} \times \cos\left(\frac{m\pi x}{a}\right)\cos\left(\frac{n\pi y}{b}\right). \quad (4)$$

Since the current is the unknown quantity of interest, and the tangential electric field is the quantity which is constrained in order to determine the current, a relationship between the electric field and the surface current density is derived.

In each of the three source-free regions (free space, dielectric, free space), the Helmholtz wave equation must be satisfied

$$\left(\nabla^2 + k^2\right)\overline{E} = 0. \quad (5)$$

Substituting (1) and (2) into (5) leads to a set of ordinary differential equations for the Fourier coefficients E_{mnx} and E_{mny}:

$$\left[\frac{d^2}{dz^2} - \left(k_x^2 + k_y^2 - k^2\right)\right]E_{mnx,y}(z) = 0 \quad (6)$$

where

$$k_x = \frac{m\pi}{a}, \qquad k_y = \frac{n\pi}{b}, \qquad \text{and} \qquad k = \frac{2\pi}{\lambda}. \quad (7)$$

The solutions to these homogeneous differential equations for each of the three regions include undetermined constants which are later found by applying boundary conditions. Also, in each region the z-directed electric field and the magnetic field components may be found using $\nabla\cdot\overline{E} = 0$ and $\nabla\times\overline{E} = -j\omega\mu\overline{H}$, respectively.

Now that the expressions for all of the electric and magnetic field components in each of the three regions are formulated, the undetermined constants can be found by applying the boundary conditions at the dielectric interfaces

$$\overline{n}\times\left(\overline{E}_1 - \overline{E}_2\right) = 0 \quad \text{and} \quad \overline{n}\times\left(\overline{H}_1 - \overline{H}_2\right) = \overline{J}_s. \quad (8)$$

Since the Fourier series representation for a periodic function is unique, these boundary conditions must hold for each component of the series, resulting in a system of equations relating the undetermined constants for the electric field Fourier coefficients E_{mn} to the surface current density Fourier coefficients J_{mn}. This system is solved analytically, yielding the following expressions for the relationship between the Fourier coefficients for the tangential electric fields and the surface current densities at both dielectric interfaces:

$$E_{fmnx} = j\omega\mu\left[J_{fmnx}\left(\frac{A_1}{D_1} + \frac{A_2}{D_2}\right) + J_{bmnx}\left(\frac{A_1}{D_1} - \frac{A_2}{D_2}\right) + J_{fmny}\left(\frac{A_3}{D_1} + \frac{A_4}{D_2}\right) + J_{bmny}\left(\frac{A_3}{D_1} - \frac{A_4}{D_2}\right)\right] \quad (9)$$

where

$$A_1 = u_0\left(k_x^2 - k_d^2\right)\alpha + u_d\left(k_x^2 - k_0^2\right) \quad (10)$$

$$A_2 = \left[u_0\left(k_x^2 - k_d^2\right) + u_d\left(k_x^2 - k_0^2\right)\alpha\right]\alpha \quad (11)$$

$$A_3 = -k_x k_y\left[u_0\alpha + u_d\right] \quad (12)$$

$$A_4 = -k_x k_y\left[u_0 + u_d\alpha\right]\alpha \quad (13)$$

$$D_1 = 2\left\{u_0 u_d\left[k_0^2 + k_d^2\alpha^2\right] + \left[\left(k_0^2 + k_d^2\right)\left(k_x^2 + k_y^2\right) - 2k_0^2k_d^2\right]\alpha\right\} \quad (14)$$

$$D_2 = 2\left\{u_0 u_d\left[k_0^2\alpha^2 + k_d^2\right] + \left[\left(k_0^2 + k_d^2\right)\left(k_x^2 + k_y^2\right) - 2k_0^2k_d^2\right]\alpha\right\} \quad (15)$$

$$u_0 = \sqrt{k_x^2 + k_y^2 - k_0^2} \qquad u_d = \sqrt{k_x^2 + k_y^2 - k_d^2}$$

$$\alpha = \tanh\left(\frac{u_d h}{2}\right) \quad (16)$$

$$k_0 = \omega\sqrt{\mu_0\epsilon_0} \qquad k_d = \omega\sqrt{\mu_0\epsilon_r\epsilon_0}. \quad (17)$$

The subscripts f and b in the above equations indicate a quantity on the front-side and back-side dielectric interfaces, respectively, and h is the thickness of the dielectric substrate. Similar expressions are found for the other tangential electric field components, E_{fmny}, E_{bmnx}, and E_{bmny}.

A similar, but somewhat more complicated relationship has also been derived for the case when there is a mirror placed at an arbitrary distance behind the dielectric and parallel to it. The mirror is accounted for by placing a perfectly conducting surface a prescribed distance behind the dielectric in the extended unit cell. Instead of applying the radiation condition (no incoming wave from $z = -\infty$) behind the grid, the tangential electric field is forced to be zero at the plane of the mirror, yielding a different relationship between the electric field and the surface current density.

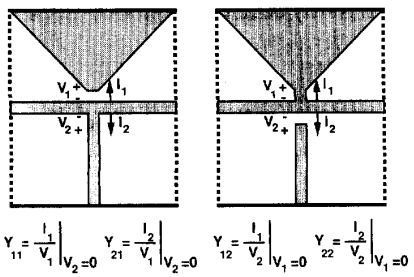

Fig. 2. For a two-port device embedded in the grid, the embedding circuit Y-parameters are found by first driving gap 1 with a generator V_1 and gap 2 short-circuited, and then driving gap 2 with a generator V_2 and gap 1 short-circuited.

B. Moment Method Solution for the Current

To determine the surface current density for a specific structure, the moment method is applied. The arbitrary metallization and the gap region are divided into a number of subdomain rooftop basis functions. The current is expressed as (assuming for simplicity that there is metal on only one side of the dielectric)

$$J_{x,y}(x,y) = \sum_{i=1}^{N_{x,y}} J_{ix,y} R_{ix,y}(x,y). \tag{18}$$

Here, J_{ix} and J_{iy} are unknown (complex) constants and R_{ix} and R_{iy} are standard rooftop basis functions in the x and y directions. The electric field coefficients E_{mnx} and E_{mny} are given in terms of J_{mnx} and J_{mny}, which are in turn determined by summing the Fourier series coefficients for the individual rooftop basis functions R_{ix} and R_{iy}

$$J_{mnx} = C_x \sum_{i=1}^{N_x} J_{ix} \sin\left(\frac{m\pi x_i}{a}\right) \sin\left(\frac{n\pi y_i}{b}\right) \tag{19}$$

where

$$C_x = \frac{2\Delta^2}{ab} \mathrm{sinc}^2\left(\frac{m\pi\Delta}{4a}\right) \mathrm{sinc}\left(\frac{n\pi\Delta}{2b}\right) \tag{20}$$

and similar expressions hold for J_{mny}. In these equations, (x_i, y_i) is the center and Δ is the width of the i^{th} square rooftop basis function. By doing this, the tangential electric field is now given in terms of the unknown constants J_{ix} and J_{iy}, which are the quantities needed to determine the driving-point impedance.

The tangential electric field must be zero on the metallization and is assumed to be constant in the small region of the gap. For a y-directed field in the gap, the constraints are

$$E_x(x,y) = \begin{cases} 0 & \text{on the metal} \\ 0 & \text{in the gap} \end{cases}$$
$$E_y(x,y) = \begin{cases} 0 & \text{on the metal} \\ 1 & \text{in the gap} \end{cases}. \tag{21}$$

The method of moments is used to set up a system of equations for the current density coefficients J_{ix} and J_{iy}. Both sides of the equations in (21) are multiplied by a number of rooftop weighting functions and then integrated over the surface area of the unit cell (Galerkin's method). This results in a system of linear equations which is solved using an LU decomposition to determine the current constants J_{ix} and J_{iy}.

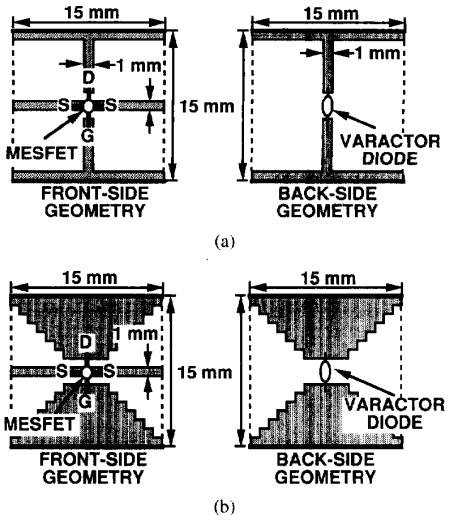

Fig. 3. Two different VCO grid unit cell geometries, (a) one with narrow-strip radiating elements and (b) another with approximated short bow-tie radiating elements. Both structures are printed on 1.0 mm thick substrates with $\epsilon_r = 2.2$. TheMESFET metallization is on one side, and the diode metallization on the other side of the dielectric substrate.

C. Driving-Point Impedance Calculation

Once the current on the structure has been found, the driving-point impedance is calculated as the ratio of the voltage across the gap to the current through the generator driving the gap. This entire analysis is performed over a range of frequencies, yielding a frequency-dependent characterization of the passive grid geometry with a single gap.

In power-combining grids demonstrated to date [1], [10], [11], the active devices are transistors (MESFET, HEMT, or HBT) which are treated here as two-port devices. Therefore, there are two gaps in the metallization, one for each port, and the analysis is performed twice. First, gap 1 is driven with a generator with gap 2 short-circuited (metallized), and then gap 2 is driven with gap 1 metallized, as shown in Fig. 2. Since the current on the entire structure is calculated for each case, two-port Y-parameters can be determined and converted to two-port S-parameters. This methodology can be extended to multi-port structures, such as a three-port voltage-controlled oscillator, in which a MESFET is located on the front-side metallization and a varactor diode on the back-side metallization, as shown in Fig. 3.

III. Prediction of Oscillation Frequency

Once the grid geometry has been characterized, the resulting n-port network can be connected to appropriate circuit models for the active device(s), and commercially available software used to simulate the grid oscillator circuit. Either a linear small-signal analysis or a nonlinear analysis can be performed. When using a linear analysis, the frequency of oscillation

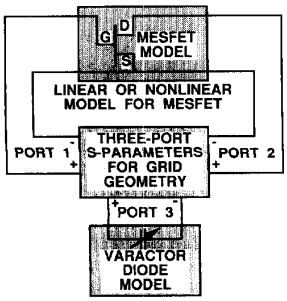

Fig. 4. The circuit used to calculate the open-loop gain of the oscillator grids. Three-port S-parameters calculated using the full-wave analysis represent the grid geometry, small-signal S-parameters are used to represent the Fujitsu FSC10LG MESFET on the front-side metallization, and a simple 0.5–pF capacitor is used to model the reverse-biased varactor diode on the back-side metallization.

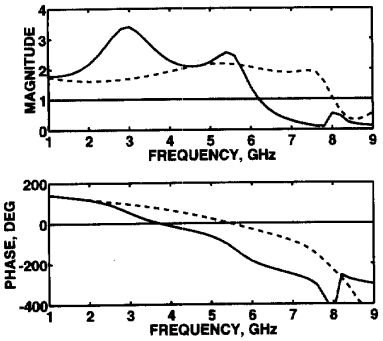

Fig. 5. The magnitude and phase of the open-loop gain for the two different VCO grid geometries shown in Fig. 3. The solid line corresponds to the geometry of Fig. 3(a) and the dashed line corresponds to the geometry of Fig. 3(b).

occurs where the open-loop gain of the circuit has magnitude greater than unity and zero phase. As an example, the S-parameters for the two different grid geometries shown in Fig. 3 are computed by the above method. Identical devices (a Fujitsu MESFET on the front side and a varactor diode on the back side) are then connected to the two grids as shown in Fig. 4, and the simulated open-loop gain obtained using *Puff* [12] for both cases is shown in Fig. 5. The simulated oscillation frequency is 3.7 GHz for the grid with narrow-strip radiating elements and 5.4 GHz for the grid with approximated bow-tie radiating elements. It is clearly seen that the metal geometry itself significantly affects the operation of the grid oscillator. For characterizing the VCO performance, the loop gain is calculated for a different value of varactor diode capacitance in the approximated bow-tie grid. Changing the diode capacitance from 0.5 pF to 2.0 pF shifts the oscillation frequency from 5.4 GHz to 4.9 GHz, yielding a 10% tuning bandwidth for a 4:1 change in diode capacitance. These results qualitatively agree with the experimental data presented in [9].

Two oscillator grids were designed and fabricated using this analysis and are given as examples. The single-sided grid metallization shown in Fig. 6 is fabricated on a 2.54–mm

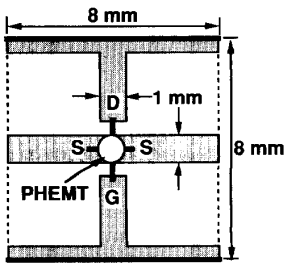

Fig. 6. A single-sided PHEMT grid oscillator unit cell geometry with narrow-strip radiating elements, printed on a 2.54–mm thick Duroid substrate with $\epsilon_r = 10.5$.

TABLE I
COMPARISON BETWEEN THE SIMULATED AND MEASURED OSCILLATION FREQUENCIES FOR THE PHEMT GRID OSCILLATOR OF FIG. 6 IN FOUR DIFFERENT CONFIGURATIONS. THE EFFECTIVE RADIATED POWER (ERP) WAS MEASURED IN THE FAR FIELD. THE SIMULATED OPEN-LOOP GAIN IS GIVEN IN THE LAST COLUMN

Grid Description	Measured Frequency	Simulated Frequency	Percentage Difference	ERP	Open-Loop Gain
2.54 mm Substrate \ Mirror	4.70 GHz	3.77 GHz	19.8%	18 dBm	11.2 dB
5.08 mm Substrate \ Mirror	3.44 GHz	3.45 GHz	0.0%	16 dBm	8.2 dB
2.54 mm Substrate \ 12.70 mm Stycast \ Mirror	3.93 GHz	3.87 GHz	1.5%	31 dBm	10.6 dB
2.54 mm Substrate \ 19.05 mm Stycast \ Mirror	4.78 GHz	4.52 GHz	5.4%	32 dBm	11.1 dB

$\epsilon_r = 10.5$ Duroid substrate with packaged Avantek ATF 35576 PHEMT's in a 5 × 5 grid oscillator. The oscillation frequency of this power combiner is simulated and measured for four different configurations: 1) with a mirror placed directly on the back of the 2.54–mm Duroid substrate, 2) with a mirror placed behind a 5.08–mm Duroid substrate, and with a 3) 12.70–mm and 4) 19.05–mm $\epsilon_r = 10$ Stycast slab backed by a mirror placed behind the 2.54–mm Duroid substrate. The open-loop gains for all four of these cases are simulated using small-signal S-parameters for the PHEMT in conjunction with the S-parameters computed for the passive part of the grid. The actual oscillation frequency of the grid in all four configurations was then measured using a broadband horn antenna in the far field and an HP 8593 spectrum analyzer. Comparisons between the simulated open-loop gains and measured oscillation frequencies are presented in Table I. Note that even though the grid metallization and the device are exactly the same in the four cases, the frequency of oscillation changes for different dielectrics and mirror positions. For the case when a mirror is placed directly behind an electrically thin substrate (approximately 0.13 λ_d in the first configuration), the disagreement between simulation and measurement is as much as 20%. This is possibly due to poor coupling between individual oscillators, which perturbs the boundary conditions.

The grid oscillator shown in Fig. 6 uses narrow-strip radiating elements and can be analyzed using the EMF method presented in [6], [8]. In Fig. 7, the rectangular unit cell geometry for a grid with one dipole and one bow-tie radiating element is shown. This grid is fabricated on a 2.54–mm $\epsilon_r =$

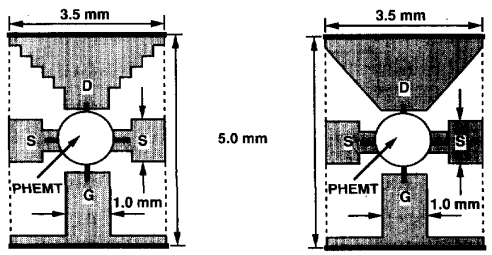

(a) (b)

Fig. 7. A single-sided PHEMT grid oscillator unit cell geometry with one narrow-strip radiating element and one bow-tie radiating element, printed on a 2.54–mm thick Duroid substrate with $\epsilon_r = 10.5$. The (a) simulated and (b) fabricated rectangular unit cell geometries are shown.

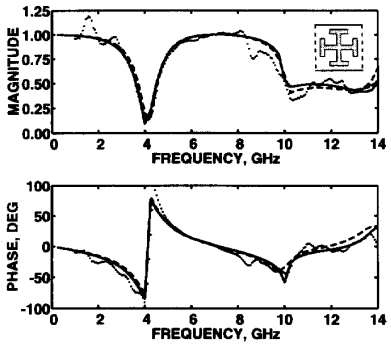

Fig. 8. The transmission coefficient of an array of Jerusalem crosses. The solid line represents the full-wave theory presented here, the dashed line represents the theory presented in [13], the dotted line represents the measured results, and the unit cell of the structure is shown in the inset.

10.5 Duroid substrate and Avantek ATF 35576 PHEMT's are used. Linear simulations predict an oscillation frequency of 9.30 GHz with an open-loop gain of 7.8 dB at 0° phase when a mirror is placed 5.0 mm behind the dielectric. The measured oscillation frequency is 9.95 GHz, a 6.5% difference. An effective radiated power of 25 dBm was measured in the far field, and should be divided by the antenna gain of the grid to get the total radiated power. This 6×4 grid has a period of $0.116\lambda_0$ in the x direction and $0.165\lambda_0$ in the y direction, and is only $0.70\lambda_0 \times 0.66\lambda_0$ in cross-section. Assuming the grid is a uniform sheet radiator, its effective area is $0.46\lambda_0^2$, which corresponds to a directivity of 7.6 dB.

IV. Reflection Coefficient Calculations

In addition to driving-point impedance calculations, it is also useful to calculate the reflection coefficient of passive periodic structures under normally incident plane wave illumination (e.g., for quasi-optical filters used in far-infrared applications). Since reflection coefficient data from passive grids are more readily available, they provide a useful verification tool for the analysis presented here.

For passive structures, there is no device driving the current on the metallization. Instead, a plane wave is assumed to be incident on the metal pattern in free space without the dielectric slab present. The current induced on the metal in turn re-radiates a reflected field. Since the total tangential electric field on the metallization must be zero, the boundary condition requires that the reflected electric field be equal and opposite to the incident field on the metal. This reflected electric field is used to determine the surface current density by the technique discussed in Section II. The TEM component of the re-radiated electric field is computed from the current distribution, and the reflection coefficient is then calculated. Transmission-line analysis is used to include the effect of the dielectric slab. The metal pattern is modelled as a frequency-dependent shunt admittance which gives the same reflection coefficient in a 377–Ω transmission line, and the dielectric is modelled as a transmission line of the appropriate characteristic impedance and length. Reflection and transmission coefficients of this transmission-line circuit are then calculated.

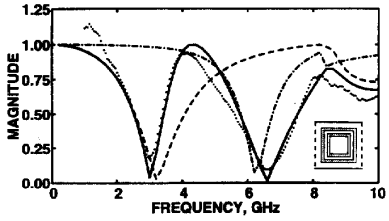

Fig. 9. The transmission coefficient of a diplexer consisting of an array of nested square loops. The solid line represents the full-wave theory presented here, the dotted line represents the measured results, the dashed line and dot-dashed lines represent the transmission coefficient of the large and small square loops alone, respectively, and the unit cell of the structure is shown in the inset.

A series of transmission coefficient measurements were performed using an HP 8510 network analyzer and two broadband horn antennas. The transmission coefficients of the structures are also computed using the full-wave analysis presented here, as well as the moment method presented in [13] for the crossed dipole and Jerusalem cross arrays. First, an array of crossed dipoles was fabricated on mylar and the comparison between measurement and the two theories is excellent. Then horizontal stubs were added on the end of the vertical dipole elements and both simulated and measured results indicate that these horizontal stubs decrease the first resonant frequency of the structure from 6 GHz to 4 GHz [14]. Finally, vertical stubs were added on the end of the horizontal dipole elements as well, resulting in an array of Jerusalem crosses. The transmission coefficients for this array are shown in Fig. 8, with the unit cell for this structure shown as an inset. The addition of these vertical stubs does not affect the first resonance, but it does introduce a rather broad frequency range over which most of the power is reflected. An example of a different diplexer designed using our theory is shown in the inset of Fig. 9. The solid line and the dotted line represent the simulated and measured transmission coefficient of the structure, respectively. The dashed line represents the simulated transmission coefficient of the larger square loops alone and the dot-dashed line represents the simulated transmission coefficient of the smaller square loops alone.

With the full-wave analysis presented here, it is possible to compute the electric field at any point in space once the current on the metal structure has been determined. For example,

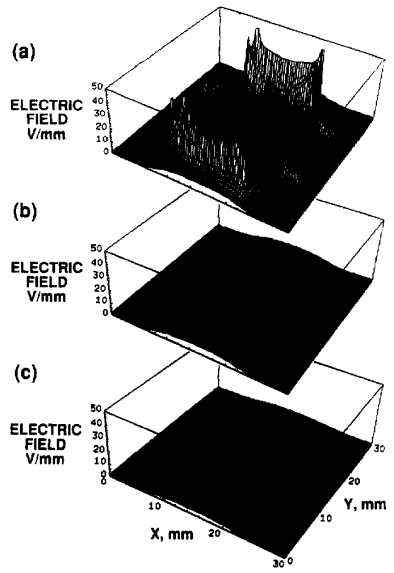

Fig. 10. Surface plots representing the magnitude of the total tangential electric field reflected from an array of Jerusalem crosses. The plots indicate the distribution of the electric field across a single unit cell of the array in different planes of constant z: (a) in the plane of the array itself, as well as (b) 1 mm and (c) 3 mm in front of the array.

the reflected electric field for some periodic array may be plotted in different planes of constant z. Field plots have been generated for the electric field reflected from an array of Jerusalem crosses (the unit cell of which is shown as an inset in Fig. 8) and are shown in Fig. 10. These surface plots represent the magnitude of the tangential part of the reflected electric field across the unit cell extended into different planes of constant z. Fig. 10(a) shows the field distribution in the plane of the array itself. It is seen that there are strong localized electric fields normal to the edges of the metallization, and so both x- and y-directed components of the field are significant. Fig. 10(b) and (c) shows the field distribution at distances of 1 mm and 3 mm from the array, respectively. The electric field distribution becomes smooth and eventually constant (a y-directed TEM mode electric field) as the observation plane moves away from the array.

V. Conclusion

A full-wave analysis of active quasi-optical grid power combiners is presented. The grid can have an arbitrary periodic metal pattern printed on either one or both sides of a dielectric. The analysis provides an embedding equivalent circuit for any multi-port active device loading the grid unit cell, and this circuit can then be analyzed using standard techniques. Several examples of MESFET and PHEMT grid oscillators are presented and clearly show that the metal shape of the grid structure, the dielectric, and the mirror all influence the oscillation frequency. As a verification of the method, transmission coefficients for several passive metal grids are calculated and compared to measurement, as well as other theories, with good agreement. The theory can be extended to any periodic quasi-optical power combiner and should prove to be a useful tool in the design and optimization of these devices.

References

[1] Z. B. Popović, M. Kim, and D. B. Rutledge, "Grid oscillators," *Int. J. Infrared Millimeter Waves*, vol. 9, no. 7, pp. 647–654, 1988.
[2] R. M. Weikle II, M. Kim, J. B. Hacker, M. P. DeLisio, Z. B. Popović, and D. B. Rutledge, "Transistor oscillator and amplifier grids," *Proc. IEEE*, vol. 80, pp. 1800–1809, Nov. 1992.
[3] J. Birkeland and T. Itoh, "A 16-element quasi-optical FET oscillator power-combining array with external injection locking," *IEEE Trans. Microwave Theory Tech.*, vol. 40, pp. 475–481, Mar. 1992.
[4] R. A. York and R. C. Compton, "Quasi-optical power combining using mutually synchronized oscillator arrays," *IEEE Trans. Microwave Theory Tech.*, vol. 39, pp. 1000–1009, June 1991.
[5] Z. B. Popović, T. B. Mader, and E. Gyorko, "Active MESFET patch oscillators and amplifiers," *24th Annu. General Assembly URSI*, Kyoto, Japan, Aug. 1993.
[6] Z. B. Popović, R. M. Weikle II, M. Kim ,and D. B. Rutledge, "A 100-MESFET planar grid oscillator," *IEEE Trans. Microwave Theory Tech.*, vol. 39, pp. 193–200, Feb. 1991.
[7] J. W. Mink, "Quasi-optical power combining of solid-state millimeter-wave sources," *IEEE Trans. Microwave Theory Tech.*, vol. MTT–34, pp. 273–279, Feb. 1986.
[8] R. M. Weikle II, M. Kim, J. B. Hacker, M. P. DeLisio, and D. B. Rutledge, "Planar MESFET grid oscillators using gate feedback," *IEEE Trans. Microwave Theory Tech.*, vol. 40, pp. 1197–2003, Nov. 1992.
[9] S. C. Bundy, T. B. Mader, and Z. B. Popović, "Quasi-optical array VCO's," *IEEE MTT-S Symp. Dig.*, June 1992, pp. 1539–1542.
[10] H. M. Harris, A. Torabi, R. W. McMillan, C. J. Summers, J. C. Wiltse, *et al.*, "Quasi-optical power combining of solid-state sources in Ka-band," *IEEE MTT-S Symp. Dig.*, June 1992, pp. 159–162.
[11] E. A. Sovero, *et al.*, "A monolithic 35 GHz HBT quasi-optical grid oscillator," *GaAs IC Symp.*, pp. 305–308, 1992.
[12] S. W. Wedge, R. Compton, and D. B. Rutledge, *Puff: Computer Aided Design for Microwave Integrated Circuits*. Pasadena, CA: California Institute of Technology, 1991.
[13] C. H. Tsao and R. Mittra, "Spectral-domain analysis of frequency selective surfaces comprised of periodic arrays of cross dipoles and Jerusalem crosses," *IEEE Trans. Antennas Propagat.*, vol. 32, pp. 478–486, May 1984.
[14] S. C. Bundy and Z. B. Popović, "Analysis of planar grid oscillators," *IEEE MTT-S Symp. Dig.*, May 1994 pp. 827–830.

Scott C. Bundy (S'92), for a photograph and biography, see this issue, page 2485.

Zoya B. Popovic, for a photograph and biography, see page 1826 of the September issue of this TRANSACTIONS.